Thermoelectric transport in Weyl semimetal $BaMnSb_2$: A first-principles study

Yubi Chen [1,2] Rongying Jin [3] Bolin Liao [2,*] and Sai Mu [3,†]

[1]*Department of Physics, University of California, Santa Barbara, California 93106-9530, USA*

[2]*Department of Mechanical Engineering, University of California, Santa Barbara, California 93106-5070, USA*

[3]*SmartState Center for Experimental Nanoscale Physics, Department of Physics and Astronomy, University of South Carolina, South Carolina 29208, USA*

(Received 10 March 2024; accepted 16 July 2024; published 15 August 2024)

Topological materials are often associated with exceptional thermoelectric properties. Orthorhombic $BaMnSb_2$ is a topological semimetal consisting of alternating layers of Ba, Sb, and MnSb. A recent experiment demonstrates that $BaMnSb_2$ has a low thermal conductivity and modest thermopower, promising as a thermoelectric material. Through first-principles calculations with Coulomb repulsion and spin-orbit coupling included, we studied the electronic structure, phononic structure, and thermoelectric transport properties of $BaMnSb_2$ in depth. We find that $BaMnSb_2$ exhibits a low lattice thermal conductivity, owing to the scattering of the acoustic phonons with low-frequency optical modes. Using the linearized Boltzmann transport theory with a constant relaxation time approximation, the thermopower is further calculated and an intriguing goniopolar transport behavior, which is associated with both *n*-type and *p*-type conduction along separate transport directions simultaneously, is observed. We propose that the figure of merit can be enhanced via doping in which electrical conductivity is increased while the thermopower remains undiminished. $BaMnSb_2$ is a potential platform for elucidating complex band structure effects and topological phenomena, paving the way to explore rich physics in low-dimensional systems.

DOI: 10.1103/PhysRevMaterials.8.085401

I. INTRODUCTION

Topological materials emerged as a fascinating class of materials in condensed matter physics, holding promise for applications such as spintronics and quantum computation [1–3]. Recently, there has been a growing interest in the research of topological thermoelectrics, focusing on novel topological materials for thermoelectric energy conversion [4,5]. For topological insulators, there are various properties desirable for thermoelectric applications: electronic energy bands with linear dispersions for high carrier mobility, low thermal conductivity due to heavy elements and lattice instability [6], a small band gap due to strong spin-orbit coupling, and the topologically protected surface states that are stable against backscattering and defects [4,5]. For topological semimetals, Skinner and Fu first theoretically proposed the nonsaturating thermopower in a magnetic field [7]. Experiments have confirmed that the Seebeck coefficient of topological semimetals can increase without saturation with magnetic field [8,9]. It has also been suggested that, close to topological phase transitions of topological materials, the thermal conductivity is reduced owning to the Kohn-anomaly-induced phonon softening by first-principles simulations, Raman spectroscopy, x-ray scattering, and neutron scattering, opening up a possibility to further enhance the thermoelectric performance [6,10,11]. The above properties of topological materials are promising features for improving the thermoelectric energy conversion efficiency. So far, the electronic properties of topological insulators and semimetals have been extensively explored [6,10], but the thermal transport properties of topological materials are less investigated. In this work, we focus on lattice vibrations and thermal transport properties of $BaMnSb_2$ and its potential thermoelectric applications. By focusing on the lattice vibrations and thermal transport properties of $BaMnSb_2$, our study aims to deepen the understanding of heat conduction mechanisms in topological insulators and semimetals.

$BaMnSb_2$ is an orthorhombic topological semimetal composed of alternating layers of Sb, Ba, and MnSb [see Fig. 1(a) for structural illustration]. $BaMnSb_2$ was previously assigned to a tetragonal structure with a Sb square net [12]. Based on the first-principles calculations of the Sb square net structure, Farhan *et al.* [13] predicted that the Dirac fermions exist. Liu *et al.* [14] and Huang *et al.* [15] reported the experimental discovery of $BaMnSb_2$ hosting nearly massless fermions with high mobility and a nontrivial Berry phase. However, recent studies identified a small orthorhombic distortion on the Sb layer, with space group $Imm2$ and $a = 4.4583$ Å, $b = 4.5141$ Å, and $c = 24.2161$ Å [16]. The distortion induces a zigzag chainlike structure on the Sb layer, opening a gap for the Dirac fermions and leading to spin-valley locking [16,17]. The signature of electronic band structure near the Fermi level is further confirmed by high-resolution angle-resolved photoemission spectroscopy measurements [18]. In $BaMnSb_2$, the charge dynamics [19], surface morphology [20], pressure dependence [21], and phonon helicity [22] have also been explored to reveal the rich physics of this material. Recent experiments [23] have demonstrated that $BaMnSb_2$ exhibits

*Contact author: bliao@ucsb.edu

†Contact author: mus@mailbox.sc.edu

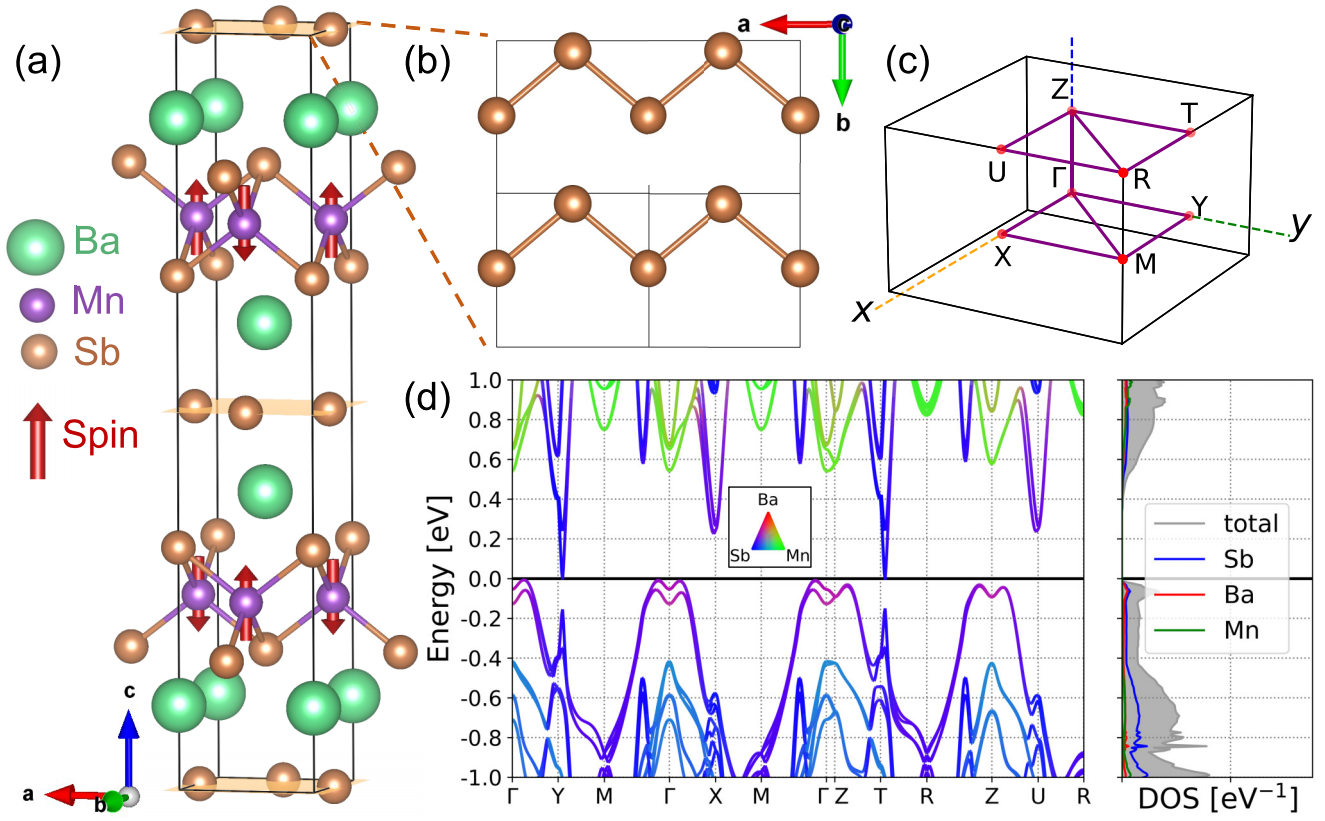

FIG. 1. (a) The atomic structure of orthorhombic $BaMnSb_2$, comprised of alternative stacking of Ba, Sb, and MnSb layers. The Mn atoms carry spin $S = 5/2$ with a G-type antiferromagnetic spin structure. The red arrows denote spins. Green, purple, and brown spheres denote Ba, Mn, and Sb atoms, respectively. (b) The zigzag structure of the Sb layer. (c) The Brillouin zone of an orthorhombic structure with selected **k** points. The purple lines include two **k**-point paths differing in z direction: Γ-Y-M-Γ-X-M and Z-T-R-Z-U-R. (d) The band structure and element-projected density of states (DOS) of $BaMnSb_2$ using PBE + U + SOC. The color bar encodes the atomic nature of the electron states.

the low thermal conductivity and modest thermal power, making it a potential candidate for thermoelectric application. However, despite extensive experimental studies, a thorough computational investigation of lattice vibration of $BaMnSb_2$ remain unexplored, and it is interesting to look into the thermal transport properties of this topological material because of its possible peculiar thermal transport behavior.

In this study, we aim to provide a detailed first-principles analysis of $BaMnSb_2$ electronic structure, phononic structure, and thermoelectric transport properties, which are pivotal to understand and optimize the thermoelectric performance of this material. To delve into the underlying physics of $BaMnSb_2$ thermal transport properties, we employ density functional theory (DFT) to investigate the electronic and phononic structures, taking into account the on-site Coulomb repulsion for $3d$ orbitals and spin-orbit coupling, which are important for this material. We reveal that the orthorhombic distortion of the Sb layer stabilizes the lattice of $BaMnSb_2$ and opens a gap in the electronic band structure, providing another example of lattice instability near a topological phase transition [6]. Employing the anharmonic three-phonon scattering and semiclassical Boltzmann theory, we obtain the phonon and electron transport properties of $BaMnSb_2$, and explore the strategies to increase the thermoelectric figure of merit through alloying. The thermoelectric behavior of $BaMnSb_2$ is intricately linked to its topological properties, specifically exhibiting goniopolar characteristics due to these properties. The comprehensive study on the thermal transport properties of $BaMnSb_2$ provides insights into the enhancement of thermal power, with potential applications in a variety of energy-efficient technologies.

This paper is organized as follows: Sec. II outlines the computational methodology employed for our first-principles calculations, including DFT, phonon dispersion calculations, and electron transport properties. In Sec. III, we present and discuss our results, focusing on the electronic structure, ground states, phonon dispersion under various distortions, and phonon and electron transport of $BaMnSb_2$. Section IV concludes this paper.

II. METHODOLOGY

A. Computational details

First-principles calculations were performed in Vienna *Ab initio* simulation package (VASP) version 6.3.1 [24,25] using projector augmented wave potentials [26]. For Ba, the valence electrons consist of $5s^2 6p^6 6s^2$ orbitals; for Mn, $3p^6 3d^5 4s^2$ orbitals; and for Sb,$5s^2 5p^3$ orbitals. A plane-wave basis set with a kinetic energy cutoff of 400 eV was utilized, and Gaussian smearing was applied with a broadening of 0.01 eV. For the unit cell, a Monkhorst-Pack [27] $12 \times 12 \times 6$ **k**-point mesh is used for Brillouin zone integration.

Convergence criteria were set to 1×10^{-8} eV for total energy and 0.001 eV/Å for the Hellmann-Feynman force on each atom. The Perdew-Burke-Ernzerhof (PBE) exchange–correlation functional was employed for calculations [28]. The on-site Coulomb interaction (U) on Mn $3d$ orbitals was described by the spherically averaged DFT + U method [29], in which the Hamiltonian only depends on U_{eff}. U_{eff} was set to 5 eV, which was determined using the linear response theory [30] and is in line with reported values in other studies [13,31]. The spin-orbit coupling (SOC) and PBE + U are included for band structure and thermal calculations [see Fig. S1(a) in the Supplemental Material for the influence of SOC on the electronic band structure [32]]. The PBE + U + SOC calculation employs a smaller **k** grid Γ-centered $7 \times 7 \times 3$ to compromise the computational expense.

B. Phonon transport

The phonon properties of the material were calculated using PHONOPY [33] based on the Hellmann-Feynman forces [34]. The input interatomic force constants were obtained from VASP calculations. 64-atom supercells with dimension of $2 \times 2 \times 1$ are generated for finite-displacement calculations, and the default atomic displacement amplitude (0.01 Å) is applied. It has been demonstrated that the phonon bands have already been converged under this default displacement in phonon calculations. A Monkhorst-Park $4 \times 4 \times 1$ **k**-mesh grid was used in the supercells to ensure the convergence of the phonon dispersion.

We calculated the lattice (phonon-contributed) thermal conductivity κ_{ph} by iteratively solving the phonon Boltzmann transport equation using SHENGBTE including the isotope-scattering effect [35]. The second-order and third-order calculations with five neighbors are first performed with PBE + U and PBE + U + SOC to show the independence of the SOC, as illustrated in Supplemental Material Fig. S1 [32]. The third-order calculations employ nine neighbors with 1756 finite-displacement jobs under the PBE + U functional. The convergence with respect to the number of neighbors is shown in Supplemental Material Fig. S1(d) [32]. The supercell size and **k**-grid sampling of third-order calculations are consistent with the second-order calculations. The broadening parameter in SHENGBTE is chosen as 0.1 and the **q**-mesh grid used is $10 \times 10 \times 10$. The convergence test of the broadening parameter and **q**-mesh grid induces less than 0.05 $\text{W m}^{-1}\text{ K}^{-1}$ (3% in the in-plane direction and 6% in the z direction) difference in thermal conductivity.

We also checked the phonon bands under different magnetic ordering, which provides insights into the coupling between lattice and spin degree of freedom (see Sec. III in the Supplemental Material and Fig. S5 [32]). We found the phonon bands, particularly in the low-frequency region, are inert to the magnetic ordering, suggesting that the magnon-phonon coupling and its potential influence on thermal transport are weak.

C. Electron transport

We consider electron transport by the linearized Boltzmann transport equation using BOLTZTRAP [36,37], where the collision term is given by the constant relaxation time approximation. The PBE + U + SOC electronic band structures obtained from the VASP calculations on a Γ-centered $62 \times 62 \times 10$ **k** grid served as input for BoltzTraP. The Fermi surface is then Fourier interpolated [36,37] on a Γ-centered $201 \times 199 \times 38$ **k** grid. The output properties calculated using BOLTZTRAP in this work are thermopower and Hall carrier concentrations, which do not depend on the relaxation time within the constant relaxation time approximation. See Supplemental Material [32] Sec. I for details to modify BOLTZTRAP to facilitate the convergence of transport properties and the comment on phonon drag effect (see also Refs. [38,39] therein).

TABLE I. The calculated lattice parameters of $BaMnSb_2$ unit cell, compared to the experiment [16]. The total energies of the G-type antiferromagnetic states for different spin quantization axes using PBE + U + SOC. All energies are referenced to the case of the spin quantization axis along z.

Lattice parameter	a	b	c
Calc. (Å)	4.5563	4.6120	24.8195
Expt. (Å) [16]	4.4583	4.5141	24.2161
Spin quantization axis	x-[100]	y-[010]	z-[001]
Energy (meV/f.u.)	0.284	0.307	0.00

III. RESULTS AND DISCUSSIONS

A. Ground state of $BaMnSb_2$

In this section, we present the results of our first-principles calculations for the electronic ground state of $BaMnSb_2$.

The orthorhombic $BaMnSb_2$ atomic structure is shown in Fig. 1(a). $BaMnSb_2$ is comprised of the alternative stacking of Ba, Sb, and MnSb layers. The calculated lattice parameters are listed in Table I, which compare well with the experiment parameters. Our DFT calculations using PBE slightly overestimate the lattice parameters by 2%. The G-type antiferromagnetic state is the ground state [see red arrows in Fig. 1(a) for the spin configuration], and our calculated spin moment on Mn is 4.55 μ_B ($S = 5/2$), in a high spin state with a half-filled d shell. All spins are found to be aligned along the c axis [14]. The calculated magnetic properties are consistent with those reported in Refs. [14, 16]. To verify the spin-easy axis, we further calculated the magnetocrystalline anisotropy energy (MAE) by comparing the relativistic total energies (with SOC) for different spin quantization axes (see Table I). We do observe the lowest total energy with all spins aligned along the c axis. The calculated MAE is about 0.295 meV per formula unit (f.u.). This low MAE is consistent with the reduced spin-orbit interaction for the case of a half-filled d shell ($3d^5$ for Mn cation) and the negligible orbital moment (0.01 μ_B from our calculation).

From the magnetic torque experiment, Huang *et al.* declared a notable spin canting in addition to the primary G-type antiferromagnetic order [15,23], resulting in a secondary ferromagnetic order parameter. To explore the possible spin canting, we explicitly introduce various initial spin canting patterns and converge the charge density and spin density. The

spins always relax back to the z axis precisely, maintaining a G-type antiferromagnetic ordering. Our result does not support the existence of a weak ferromagnetism.

Half-filled d shells are optimal for antiferromagnetic coupling. The measured Néel temperature of $BaMnSb_2$ is 283–286 K [14–16,23]. To estimate the magnetic transition temperature, we evaluated the exchange energy, which is defined as the energy separation between the magnetic ground state and the state in which the local moment on one Mn is flipped. In the Heisenberg model, the exchange energy E_i on site i is given by $E_i = 2\sum_j J_{ij}$, where J_{ij} is the Heisenberg exchange parameter. For the homogeneous system with equivalent magnetic sites, the mean-field T_N for the classical Heisenberg model is equal to 1/6 of the exchange energy. Our calculated exchange energy for $BaMnSb_2$ is 0.2028 eV, giving a classical mean-field temperature of 392 K. The overestimation of T_N is due to the neglect of spin correlation in a mean-field model.

Figure 1(b) provides a top view of the Sb layer in Fig. 1(a), revealing a zigzag chainlike structure in the Sb layer. The formation of zigzag distortion yields a 48.8 meV total energy reduction per formula unit compared to the high-symmetry tetragonal structure. The zigzag distortion results in a shorter bond between the two Sb atoms, which are located at (0.5,0.068,0) and (0,0.488,0) in Fig. 1(b). (Note the coordinates are in the basis of lattice vectors of the unit cell). The band structure of $BaMnSb_2$ is depicted in Fig. 1(d) and the high-symmetry $\mathbf{k}$ points are defined in Fig. 1(c). The two-dimensional k paths (Γ-Y-M-Γ-X-M and Z-T-R-Z-U-R) have very similar band structures, which correspond to the layered atomic structure in Fig. 1(a). It is worth noting that the conduction band minimum (CBM) near the Y point and the valence band maximum (VBM) near the Γ point occur at the same energy. The CBM electron state is a topological state with its wave function originating from the Sb zigzag layers. The CBM state is located at (0.049,0.5,0.5), while the VBM state is located at (0,0.13,0), both in the basis of reciprocal lattice vectors. The VBM state is topologically trivial, which is much flatter than the steep topological CBM state. The drastically different curvatures of the CBM and VBM states lead to the distinct shape of the density of states (DOS) also shown in Fig. 1(d). The lowest CB state is steep and contributes to a tiny DOS, while the VBM DOS is much larger due to the less-dispersive band curvature, which yields a Van Hove singularity. This feature is important for $BaMnSb_2$ as a potential candidate for thermoelectric applications, which will be discussed in Sec. III C.

B. Phonon transport

Now we move to the investigation of the phonon band structure of $BaMnSb_2$, which is pivotal to understand its lattice stability and thermal transport property. We first explore the importance of orthorhombic distortion in stabilizing the lattice and its impact on the electronic structure. We interpolate the structure between the tetragonal lattice (denoted as 0% distortion) and the orthorhombic lattice (denoted as 100% distortion) to acquire an intermediate configuration, which we refer to as 50% distortion. The phonon dispersion is calculated for the above three structures to explore the structural instability.

The phonon dispersions of 0%, 50%, and 100% distortion structures are shown in Fig. 2(c). The calculations are conducted using PBE + U and we have verified that PBE + U + SOC yields the same phonon structure obtained from PBE + U (see Supplemental Material Fig. S1 [32]). From Fig. 2(c), the 0% and 50% distortion structures exhibit imaginary frequencies at both Γ and Z points. With a larger distortion, the magnitude of negative frequencies gradually diminishes. The orthorhombic structure with 100% distortion is stable without any imaginary-frequency phonon modes. By visualizing the eigenvector of the soft phonon mode for 0% distortion at the Γ point [see inset of Fig. 2(c)], the vibrational movement is exclusively attributed to the two Sb atoms within the Sb layer. These two Sb atoms in Fig. 1(b) vibrate against each other along the b direction, thereby forming the zigzag distortion in the Sb layer.

To elucidate the formation mechanism of the zigzag structure, Tremel and Hoffmann [40] conducted an in-depth investigation into layered stacking structures with square atomic nets to discern the pivotal element triggering the distortion (see Supplemental Material [32] Sec. I for details). Their argument lies in whether the electron filling is close to the band crossing point in the high-symmetry square atomic net structure, as shown in Fig. 2(b). Although such a distortion from a high-symmetry configuration induces an increase in the elastic energy, it also creates a bonding/antibonding splitting from the degenerate orbitals in Fig. 2(a). With the correct electron filling—that is, the Fermi level lying close to the Dirac crossing—only the bonding states become occupied, leading to a reduction in the electron energy. This thereby gives rise to the preference for a symmetry-lowering distortion. This argument is in the same spirit as the Peierls transition [41]. The recent discovery of the distorted $BaMnSb_2$ structure revealed its proximity to the nondistorted structure, which is unstable. Hence, as displayed in Fig. 2(c), the phonon dispersion for unstable structures exhibits optical phonon modes with imaginary frequencies, and only for the fully distorted orthorhombic structure do the frequencies of those optical modes become positive. This presents an additional perspective on the lattice instability observed near the topological phase transition, as discussed in a few previous studies [6,10,11].

We further calculate the thermal conductivity of $BaMnSb_2$ using SHENGBTE. The calculated temperature-dependent thermal conductivity of the lattice along different crystallographic axes ($\kappa^a_{\rm ph}$, $\kappa^b_{\rm ph}$, and $\kappa^c_{\rm ph}$) are illustrated in Fig. 2(d). The experimentally measured in-plane thermal conductivity [23] is also shown for comparison. Note that the experimental phonon thermal conductivity is derived by subtracting the electron contribution $\kappa^{ab}_{\rm e}$ from the total thermal conductivity κ^{ab}. At low temperatures, the discrepancy in lattice thermal conductivity between the calculation and the experiment is due to the omission of the phonon-boundary scattering (the dominant scattering mechanism at low T) in the calculations [42]. At elevated temperatures, the phonon thermal conductivity is mainly limited by phonon-phonon scattering. We observe a good agreement with experimental lattice thermal conductivity near the room temperature. While the

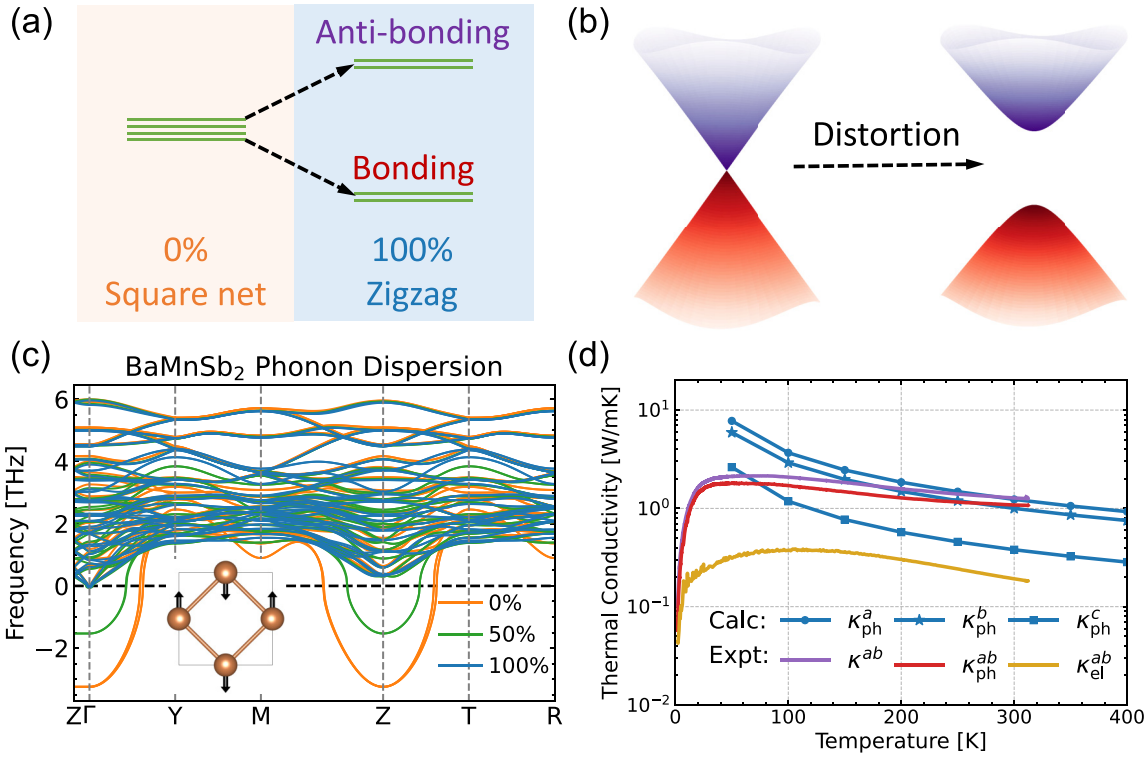

FIG. 2. (a) A sketch of band splitting into bonding-antibonding states, from the high-symmetry tetragonal Sb square net case (denoted as 0% distortion) to the low-symmetry orthorhombic Sb zigzag distortion case (denoted as 100% distortion). (b) The band visualization of the avoid crossing for the bonding-antibonding splitting. (c) The phonon dispersion under 0%, 50% (intermediate), and 100% distortion. 0% distortion exhibits imaginary phonon modes, and the magnitude of the imaginary modes gradually diminishes with larger distortion. (d) The thermal conductivity κ of $BaMnSb_2$, including electron-mediated, κ_{el}, and phonon-mediated, κ_{ph}, parts. "Calc." is the calculated phonon thermal conductivity along the a, b, c directions. "Expt." is the experimental thermal conductivity in Ref. [23].

inclusion of four-phonon scattering [43–45] could lead to more accurate results and potentially improves the agreement with experiment, it may not make notable changes for the low-symmetry $BaMnSb_2$, since the calculated thermal conductivity from the three-phonon process is already low. Therefore, the computationally expensive four-phonon scattering is not explored in the present study. At 300 K, the calculated phonon thermal conductivities are $\kappa^a_{ph} = 1.23$, $\kappa^b_{ph} = 1.00$, and $\kappa^c_{ph} = 0.38\ \mathrm{W\,m^{-1}\,K^{-1}}$. At temperatures above 300 K, the calculated thermal conductivity trend falls below the experimental one, and is probably due to the wavelike phonon-tunneling thermal conductivity [46]. The higher in-plane thermal conductivity than the out-of-plane thermal conductivity is consistent with the structural feature of these layered materials, in which the in-plane bonding is stronger than the out-of-plane bonding. There is a small in-plane anisotropy between κ^a_{ph} and κ^b_{ph} due to the orthorhombic distortion. The calculated κ^a_{ph} and κ^b_{ph} are fairly close to the experimental in-plane lattice thermal conductivity $\kappa^{ab}_{ph} = 1.08\ \mathrm{W\,m^{-1}\,K^{-1}}$.

Overall, the lattice thermal conductivities are rather low. This is due to the scattering of acoustic phonons with the low-frequency, or "soft," optical modes. Further details regarding three-phonon scattering rates and cumulative thermal conductivity can be found in Fig. S2 of the Supplemental Material [32]. While our investigation of the phonon transport properties affirms the potential of $BaMnSb_2$ as a promising thermoelectric material due to its low lattice thermal conductivity, a complete understanding of its thermoelectric performance requires a simultaneous examination of the electron transport properties, which will be the focus of the subsequent section.

C. Electron transport

We now focus on another critical facet of its thermoelectric performance—electron transport. To gain insight into electron transport, we first calculate an accurate electronic structure incorporating SOC [see Fig. 1(d)] and employ the linearized Boltzmann transport equation to assess the transport property. The constant relaxation time approximation is adopted in the process.

Figure 3(a) shows the Hall carrier concentration as a function of the Fermi level at different temperatures. The Fermi level located at $E_F = 0$ eV corresponds to the charge neutrality condition for the pristine structure. When the Fermi level E_F is moved above zero, the majority of charge carriers are electrons, while when the Fermi level E_F is moved below zero, the majority of charge carriers are holes. The sharp peaks in the Hall concentration in the $E_F < 0$ region is due to the dominant DOS of the less-dispersive top valence bands. The position of Fermi level is sample dependent and is related to the carrier concentration. In order to compare

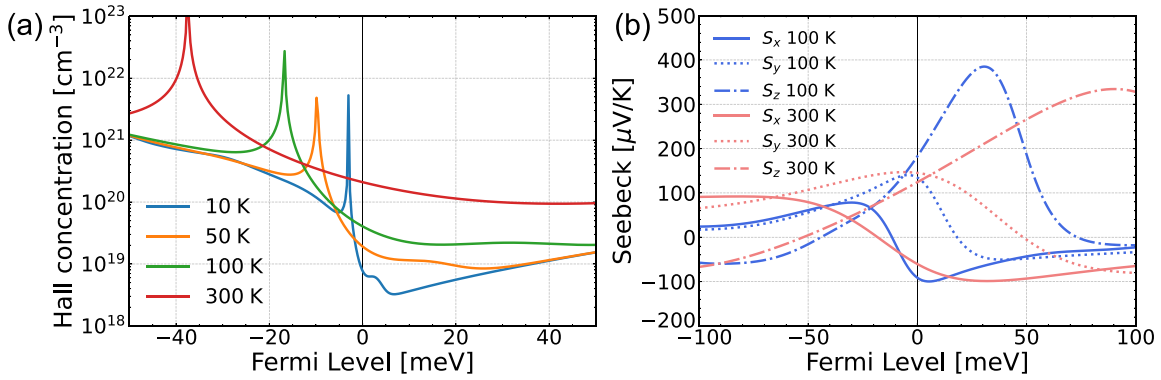

FIG. 3. Electron transport properties of $BaMnSb_2$ with constant relaxation time approximation. (a) Hall carrier concentration as a function of Fermi level. (b) The Seebeck coefficients S_x, S_y, S_z as a function of Fermi level at temperatures of 100 and 300 K.

our calculation to experimental measurements [14–17,21,23], we estimate the actual position of Fermi level by calculating the angle-dependent oscillation frequency and comparing it with the experimental Shubnikov–de Haas measurement. The measured oscillation frequency [14,15] at each angle was reproduced from our DFT calculations, only when the Fermi level is set to 35 meV (see Fig. S4 in the SM [32] for an analysis and see also Ref. [47] therein for calculation details). At this determined Fermi level, the Hall carrier concentration is about 1.0×10^{19} cm^{-3} at 10 K in Fig. 3(a). It is close to the previously reported experimental values at 10 K: 1.16×10^{19} cm^{-3} in Ref. [15] and 1.4×10^{19} cm^{-3} in Ref. [14], respectively.

Figure 3(b) illustrates the Seebeck coefficient as a function of the Fermi level at 100 and 300 K. The Seebeck coefficients along three crystallographic axes are calculated separately. In general, we anticipate a positive Seebeck coefficient ($S > 0$) for hole carriers ($E_F < 0$) and a negative one ($S < 0$) for electron carriers ($E_F > 0$), with a few examples discussed in Ref. [48]. At both temperatures ($T = 100$ K and $T = 300$ K) and for a positive E_F, $BaMnSb_2$ exhibits an intriguing goniopolar behavior [49–51], namely, the material simultaneously possesses p-type conduction along the z direction ($S_z > 0$) and n-type conduction along specific in-plane directions ($S_x < 0, S_y < 0$). This unconventional behavior can be explained by the drastically different curvatures of the electronic bands near the CBM and VBM states. As described in Sec. III A, the top of the valence band is very flat and almost dispersionless while the bottom of the CB is much sharper, leading to a large contrast in the electron and hole DOS near E_F. At higher temperatures, the Fermi-Dirac distribution broadens near the Fermi level. Given that the hole carriers have a substantially larger DOS compared to that of the electrons [see Fig. 1(d)], the holes dominate the contribution to the Seebeck coefficient, rendering a positive Seebeck even for a Fermi level deep into the conduction band. A more detailed analysis on the underlying mechanism for this distinctive behavior is elaborated in Fig. S3 of the Supplemental Material [32]. The orthorhombic distortion in $BaMnSb_2$ opens a band gap, leading to a unique electronic signature—sharp conduction bands and flat valence bands near the Fermi level—and the observed goniopolar behavior. This intriguing goniopolar behavior opens avenues for innovative electronic devices that leverage direction-dependent carrier polarity, such as thermoelectric converters, photovoltaic cells, transistors, and sensors [52–57]. Beyond this, goniopolar materials can showcase complex transport phenomena unattainable in conventional semiconductors, including anisotropic magnetoresistance, the Nernst effect, and the Hall effect. With such unique features, goniopolar materials carry immense potential to transform sectors such as electronics, energy conversion, and information technology.

Bringing together the unique electron transport behavior and the low lattice thermal conductivity, we can estimate the thermoelectric figure of merit and evaluate the potential of $BaMnSb_2$ as a thermoelectric material. To avoid the complexity of subjectively choosing an electron relaxation time, we estimate it from experimental values. The thermoelectric figure of merit is defined as $ZT = \frac{\sigma S^2 T}{\kappa}$, where S is the Seebeck coefficient, T the temperature, σ the electrical conductivity, and κ the thermal conductivity [42]. σ and κ are from experimental measurements and S is based on our DFT calculations. At room temperature (300 K), the variables are reported as follows: the in-plane thermal conductivity $\kappa = 1.3$ W/mK [23]; the in-plane Seebeck coefficient 72 μV/K [23] [within the range of Fig. 3(b)]; and the in-plane electrical conductivity $\sigma = 3.7 \times 10^4$ S/m [23] or 2×10^5 S/m [17]. Accordingly, the thermoelectric figure of merit ZT of the $BaMnSb_2$ material is either 0.03 [23] or 0.24 [17] at 300 K.

The thermoelectric performance can potentially be further enhanced by adjusting the temperature and doping levels to optimize the figure of merit. Additionally, other standard techniques, such as grain refinement and modulation doping, may also improve the figure of merit [58–60]. In light of these insights into the unique phonon and electron transport properties of $BaMnSb_2$, we foresee its potential to impact the design and experimental pursuits in thermoelectric materials. Our findings will be informative in advancing the efficient and sustainable energy solutions across diverse scientific disciplines.

IV. CONCLUSIONS

In summary, we present an in-depth first-principles study of thermal transport in the Weyl semimetal $BaMnSb_2$. We use

density functional theory to comprehensively investigate the electronic structure, phononic structure, and electron transport of $BaMnSb_2$, taking into account the effects of Coulomb repulsion and spin-orbit coupling. Our calculations reveal a low lattice-mediated thermal conductivity of $BaMnSb_2$ due to the phonon scattering by low-frequency optical phonon modes when assessing three-phonon scattering. The electron transport exhibits an unconventional goniopolar behavior of the Seebeck coefficient as a function of the Fermi level. These findings, along with the estimated figure of merit, render $BaMnSb_2$ as a potential thermoelectric material for an efficient and sustainable energy solution. We anticipate that our insights will be informative for the design and experimental realizations of thermoelectric materials towards improved performance.

ACKNOWLEDGMENTS

This work is based on research supported by the U.S. Office of Naval Research under the Award No. N00014-22-1-2262. Y.C. also acknowledges the support from the Graduate Traineeship Program of the NSF Quantum Foundry via the Q-AMASE-i program under Award No. DMR-1906325 at the University of California, Santa Barbara (UCSB). S.M. would like to acknowledge the startup fund from the University of South Carolina and an ASPIRE grant from the VPR's office at the University of South Carolina. This work used the Expanse supercomputer at the San Diego Supercomputer Center through allocation PHY230093 from the Advanced Cyberinfrastructure Coordination Ecosystem: Services & Support (ACCESS) program, which is supported by National Science Foundation Grants No. 2138259, No. 2138286, No. 2138307, No. 2137603, and No. 2138296. In addition, use was made of computational facilities purchased with funds from the National Science Foundation (CNS-1725797) and administered by the Center for Scientific Computing (CSC). The CSC is supported by the California NanoSystems Institute and the Materials Research Science and Engineering Center (MRSEC; NSF DMR 2308708) at UC Santa Barbara.

[1] M. He, H. Sun, and Q. L. He, Front. Phys. **14**, 1 (2019).
[2] Q. L. He, T. L. Hughes, N. P. Armitage, Y. Tokura, and K. L. Wang, Nat. Mater. **21**, 15 (2022).
[3] L. Šmejkal, Y. Mokrousov, B. Yan, and A. H. MacDonald, Nat. Phys. **14**, 242 (2018).
[4] C. Fu, Y. Sun, and C. Felser, APL Mater. **8**, 040913 (2020).
[5] N. Xu, Y. Xu, and J. Zhu, npj Quantum Mater. **2**, 51 (2017).
[6] S. Yue, B. Deng, Y. Liu, Y. Quan, R. Yang, and B. Liao, Phys. Rev. B **102**, 235428 (2020).
[7] B. Skinner and L. Fu, Sci. Adv. **4**, eaat2621 (2018).
[8] F. Han, N. Andrejevic, T. Nguyen, V. Kozii, Q. T. Nguyen, T. Hogan, Z. Ding, R. Pablo-Pedro, S. Parjan, B. Skinner *et al.*, Nat. Commun. **11**, 6167 (2020).
[9] W. Zhang, P. Wang, B. Skinner, R. Bi, V. Kozii, C.-W. Cho, R. Zhong, J. Schneeloch, D. Yu, G. Gu *et al.*, Nat. Commun. **11**, 1046 (2020).
[10] S. Yue, H. T. Chorsi, M. Goyal, T. Schumann, R. Yang, T. Xu, B. Deng, S. Stemmer, J. A. Schuller, and B. Liao, Phys. Rev. Res. **1**, 033101 (2019).
[11] T. Nguyen, F. Han, N. Andrejevic, R. Pablo-Pedro, A. Apte, Y. Tsurimaki, Z. Ding, K. Zhang, A. Alatas, E. E. Alp *et al.*, Phys. Rev. Lett. **124**, 236401 (2020).
[12] G. Cordier and H. Schäfer, Z. Naturforsch. B **32**, 383 (1977).
[13] M. A. Farhan, G. Lee, and J. H. Shim, J. Phys.: Condens. Matter **26**, 042201 (2014).
[14] J. Liu, J. Hu, H. Cao, Y. Zhu, A. Chuang, D. Graf, D. J. Adams, S. M. Radmanesh, L. Spinu, I. Chiorescu, and Z. Mao, Sci. Rep. **6**, 30525 (2016).
[15] S. Huang, J. Kim, W. A. Shelton, E. W. Plummer, and R. Jin, Proc. Natl. Acad. Sci. USA **114**, 6256 (2017).
[16] H. Sakai, H. Fujimura, S. Sakuragi, M. Ochi, R. Kurihara, A. Miyake, M. Tokunaga, T. Kojima, D. Hashizume, T. Muro, K. Kuroda, T. Kondo, T. Kida, M. Hagiwara, K. Kuroki, M. Kondo, K. Tsuruda, H. Murakawa, and N. Hanasaki, Phys. Rev. B **101**, 081104(R) (2020).
[17] J. Y. Liu *et al.*, Nat. Commun. **12**, 4062 (2021).
[18] H. Rong, L. Zhou, J. He, C. Song, Y. Xu, Y. Cai, C. Li, Q. Wang, L. Zhao, G. Liu, Z. Xu, G. Chen, H. Weng, and X. Zhou, Chin. Phys. B **30**, 067403 (2021).
[19] H. Yoshizawa, H. Sakai, M. Kondo, M. Ochi, K. Kuroki, N. Hanasaki, and J. Fujioka, Phys. Rev. B **105**, L241110 (2022).
[20] Q. Zou, S. Huang, W. Ko, M. Fu, Y. Yang, K. Zhao, S. R. Crittenden, E. W. Plummer, R. Jin, and Z. Gai, npj Quantum Mater. **7**, 85 (2022).
[21] X. Yin, J. Y. Liu, T. Hu, Y. L. Huang, C. Jiang, L. J. Min, P. G. Li, Z. Q. Mao, and H. Xiao, Phys. Rev. B **105**, 045123 (2022).
[22] L. H. Hu, J. Yu, I. Garate, and C. X. Liu, Phys. Rev. Lett. **127**, 125901 (2021).
[23] S. Huang, L. Xing, R. Chapai, R. Nepal, and R. Jin, Phys. Rev. Mater. **4**, 065001 (2020).
[24] G. Kresse and J. Furthmüller, Phys. Rev. B **54**, 11169 (1996).
[25] G. Kresse and J. Furthmüller, Comput. Mater. Sci. **6**, 15 (1996).
[26] P. E. Blöchl, Phys. Rev. B **50**, 17953 (1994).
[27] H. J. Monkhorst and J. D. Pack, Phys. Rev. B **13**, 5188 (1976).
[28] J. P. Perdew, K. Burke, and M. Ernzerhof, Phys. Rev. Lett. **77**, 3865 (1996).
[29] S. L. Dudarev, G. A. Botton, S. Y. Savrasov, C. J. Humphreys, and A. P. Sutton, Phys. Rev. B **57**, 1505 (1998).
[30] M. Cococcioni and S. de Gironcoli, Phys. Rev. B **71**, 035105 (2005).
[31] S. Mu and K. D. Belashchenko, Phys. Rev. Mater. **3**, 034405 (2019).
[32] See Supplemental Material at http://link.aps.org/supplemental/10.1103/PhysRevMaterials.8.085401 for details about computational setup and comments about the methodology, calculations for quantum oscillation frequency, and computed phonon bands for different spin orderings.
[33] A. Togo and I. Tanaka, Scr. Mater. **108**, 1 (2015).
[34] R. P. Feynman, Phys. Rev. **56**, 340 (1939).

[35] W. Li, J. Carrete, N. A. Katcho, and N. Mingo, Comput. Phys. Commun. **185**, 1747 (2014).
[36] G. K. Madsen and D. J. Singh, Comput. Phys. Commun. **175**, 67 (2006).
[37] G. K. Madsen, J. Carrete, and M. J. Verstraete, Comput. Phys. Commun. **231**, 140 (2018).
[38] J. Zhou, B. Liao, B. Qiu, S. Huberman, K. Esfarjani, M. S. Dresselhaus, and G. Chen, Proc. Natl. Acad. Sci. USA **112**, 14777 (2015).
[39] Y. Quan, Y. Chen, and B. Liao, Phys. Rev. B **107**, 245202 (2023).
[40] W. Tremel and R. Hoffmann, J. Am. Chem. Soc. **109**, 124 (1987).
[41] R. E. Peierls, *Quantum Theory of Solids* (Oxford University Press, New York, 1995).
[42] G. Chen, *Nanoscale Energy Transport and Conversion: A Parallel Treatment of Electrons, Molecules, Phonons, and Photons* (Oxford University Press, New York, 2005).
[43] T. Feng and X. Ruan, Phys. Rev. B **93**, 045202 (2016).
[44] T. Feng, L. Lindsay, and X. Ruan, Phys. Rev. B **96**, 161201(R) (2017).
[45] X. Yang, T. Feng, J. Li, and X. Ruan, Phys. Rev. B **100**, 245203 (2019).
[46] E. Di Lucente, M. Simoncelli, and N. Marzari, Phys. Rev. Res. **5**, 033125 (2023).
[47] P. M. Rourke and S. R. Julian, Comput. Phys. Commun. **183**, 324 (2012).
[48] D. T. Do and S. D. Mahanti, AIP Conf. Proc. **2005**, 020005 (2018).
[49] K.-i. Uchida and J. P. Heremans, Joule **6**, 2240 (2022).
[50] Y. Wang and P. Narang, Phys. Rev. B **102**, 125122 (2020).
[51] S. K. Radha and W. R. L. Lambrecht, Phys. Rev. B **101**, 235111 (2020).
[52] Z. Wu, S. Zhang, Z. Liu, E. Mu, and Z. Hu, Nano Energy **91**, 106692 (2022).
[53] X. Wu, N. Gao, H. Jia, and Y. Wang, Chem. Asian J. **16**, 129 (2021).
[54] R. Chenni, M. Makhlouf, T. Kerbache, and A. Bouzid, Energy **32**, 1724 (2007).
[55] A. R. Jordehi, Renew. Sustain. Energy Rev. **61**, 354 (2016).
[56] Y. Liu, X. Duan, H.-J. Shin, S. Park, Y. Huang, and X. Duan, Nature (London) **591**, 43 (2021).
[57] J. Vetelino and A. Reghu, *Introduction to Sensors* (CRC, Boca Raton, FL, 2017).
[58] X. Zhou, Y. Yan, X. Lu, H. Zhu, X. Han, G. Chen, and Z. Ren, Mater. Today **21**, 974 (2018).
[59] X.-L. Shi, J. Zou, and Z.-G. Chen, Chem. Rev. **120**, 7399 (2020).
[60] M. Zebarjadi, G. Joshi, G. Zhu, B. Yu, A. Minnich, Y. Lan, X. Wang, M. Dresselhaus, Z. Ren, and G. Chen, Nano Lett. **11**, 2225 (2011).